Surface Extraction from Volumetric Images Using Deformable Meshes: A Comparative Study

Jussi Tohka

DMI / Institute of Signal Processing
Tampere University of Technology
P.O. Box 553, FIN-33101,Finland
`jussi.tohka@cs.tut.fi`

Abstract. Deformable models are by their formulation able to solve surface extraction problem from noisy volumetric images. This is since they use image independent information, in form of internal energy or internal forces, in addition to image data to achieve the goal. However, it is not a simple task to deform initially given surface meshes to a good representation of the target surface in the presence of noise. Several methods to do this have been proposed and in this study a few recent ones are compared. Basically, we supply an image and an arbitrary but reasonable initialization and examine how well the target surface is captured with different methods for controlling the deformation of the mesh. Experiments with synthetic images as well as medical images are performed and results are reported and discussed. With synthetic images, the quality of results is measured also quantitatively. No optimal method was found, but the properties of different methods in distinct situations were highlighted.

1 Introduction

Deformable models are by their formulation able to solve ill-posed problems in image processing and analysis. This is due additional image independent soft and hard constraints that are set. For the surface extraction problem, these state that the resulting surface should be smooth in the basic setting. The ability to deal with noisy and poor contrast images makes three dimensional deformable surface models particularly interesting for automated medical image analysis: Obviously, the use of model-based techniques is necessary for analyzing medical images because of imaging artifacts and noise. On the other hand, large variability of biological shapes restricts the use of shape models with only few parameters. Consequently, deformable surface meshes - which can be used to extract surfaces of highly variable shapes - are popular tools in automated medical image analysis. For deformable surface models in general and their applications to medical images, see surveys [8,9].

Deformable surface meshes are polygon meshes whose geometry evolves driven by image data and shape regularity constraints starting from given initial

meshes. There are two basic approaches controlling the evolution of the mesh. The force based approach assigns an equation of motion to each vertex of the mesh (or mexel) and lets it move in a force field formed by internal and external forces. Internal forces derive from the geometry of the mesh itself. They guarantee the smoothness of the final mesh. External forces are derived from the image data and draw deformable mesh towards salient image features. On the other hand, the energy based approach assigns an energy to each mesh belonging to the set of admissible meshes. The energy is minimized and its minimum argument is the resulting mesh. Again, the energy is divided in external and internal energies. The internal energy is derived from geometry of the mesh and the external energy is derived from image data.

If the initializations for the processes are not in the close vicinity of the target, advanced solutions for both approaches are required. Especially, when images are noisy, the energy function is likely to have multiple local minima and as well equations of motion may stabilize before the correct surface has been found. Methods to minimize the energy globally have been proposed as well as techniques for constructing external forces so that they are not sensitive to image noise nor positioning of the initial surface. In this paper, a few of recent methods for minimizing energy and techniques for advanced construction of external forces are compared experimentally. We will fix the internal energy/force model and image data and see how the different methods cope given a generic (i.e automatic) but reasonable initialization. The chosen deformable meshing techniques are compared with synthetic images in order to obtain quantitative results and with medical images to link findings into real world situations. To our knowledge, this kind of empirical study does not exist in the context of deformable surface meshes. With 2-D deformable models some quantitative comparisons have been reported, at least in [3,15].

There are approaches to the problem which are relevant to the study but are intensionally left out from it. For example, algorithms based on multi-resolution image representations (see e.g. [7]) are not considered in order to keep the size of the study reasonable. The three-dimensional generalization of the snakes-algorithm [6] is not included, since its limitations are well known. Furthermore, we do not consider algorithms that automatically adapt the topology of the mesh and hence the topology of the target surface as well as the resolution of the final mesh are to be fixed in advance.

2   Deformable Surface Mesh

In this study, simplex meshes [1] are applied for surface representation. In a simplex mesh each vertex of the mesh, or mexel, has exactly three neighbors. In another words their graphs are 3-regular. Triangular meshes, which are topological duals of simplex meshes, are also often applied in deformable meshing, see e.g. [7]. Meshes are denoted by $\mathcal{M} = (\mathbf{V}, \mathcal{G})$, where $\mathbf{V} = \{\mathbf{v}_1, \ldots, \mathbf{v}_N\} \subset \mathbb{R}^3$ is set of mexels and $\mathcal{G}$ is the graph of the mesh. Three mexels adjacent to $\mathbf{v}_i$ are denoted by $\mathbf{v}_{i_j}, j = 1, 2, 3$. The unit normal to the mesh at $\mathbf{v}_i$ is denoted by $\mathbf{n}_i$.

The input for a deformable mesh, image I, is a preprocessed version of an image to be analyzed . In I voxels are given an intensity value based on their saliency, which depends on the application. For example, I can be an edge-detected version of the original image if the interest is in finding the boundary of a volumetric target. The image I is normalized to have intensity values from 0 to 1, the voxel of the highest saliency receiving the intensity value of 1.

3   Force Based Approach

The evolution of the mesh can be controlled by assigning an equation of motion to each mexel. In the general case the equation of motion is Newtonian:

$$m\ddot{\mathbf{v}}_i(t) + \gamma\dot{\mathbf{v}}_i(t) = \alpha\mathbf{F}_{int}(\mathbf{v}_i(t)) + \beta\mathbf{F}_{ext}(\mathbf{v}_i(t)), \tag{1}$$

where $\alpha, \beta, \gamma, m \in \mathbb{R}$ and t is time. In discrete form this is written as (assuming $m = 1$)

$$\mathbf{v}_i^{t+1} = \mathbf{v}_i^t + (1 - \gamma)(\mathbf{v}_i^t - \mathbf{v}_i^{t-1}) + \alpha\mathbf{F}_{int}(\mathbf{v}_i^t) + \beta\mathbf{F}_{ext}(\mathbf{v}_i^t), \tag{2}$$

with the mesh when time $t = 0$ given. When $\gamma = 1$, (2) reduces to a Lagrangian equation of motion. The internal force

$$\mathbf{F}_{int}(\mathbf{v}_i) = \frac{1}{3}\sum_{j=1}^{3}\mathbf{v}_{i_j} - \mathbf{v}_i. \tag{3}$$

The internal force (3) causes surface to shrink to a point if no external forces are present. This is sometimes useful, because it reduces sensitivity to the initialization provided that initial meshes are set outside the target.

Semi-implicit evolution equations, such as in snakes [6], are not popular with 3-D meshes. This is since in the 3-D case this involves multiplication of large matrices, which do not have a banded structure as in the 2-D case.

3.1   Delingette's External Force

A local external force model was introduced by Delingette [1]. These forces rely on a good initialization or, as in our case, shrinking effect caused by internal forces to produce acceptable results. The external force is

$$\mathbf{F}_{ext}(\mathbf{v}_i) = \mathbf{F}_{grad}(\mathbf{v}_i) + \mathbf{F}_{edge}(\mathbf{v}_i). \tag{4}$$

The gradient force

$$\mathbf{F}_{grad}(\mathbf{v}_i) = \beta_{grad}((\mathbf{m}_i - \mathbf{v}_i) \cdot \mathbf{n}_i)\mathbf{n}_i,$$

where $\mathbf{m}_i$ is the centre of the voxel of greatest intensity in $s \times s \times s$ neighbourhood of the voxel containing $\mathbf{v}_i$. We set $s = 5$. The edge force

$$\mathbf{F}_{edge}(\mathbf{v}_i) = \beta_{edge}(\mathbf{e}_i - \mathbf{v}_i),$$

where $\mathbf{e}_i$ is the center of the closest edge voxel to $\mathbf{v}_i$ along the normal $\mathbf{n}_i$. For computing $\mathbf{F}_{edge}$ a binary edge-image, where each voxel is classified either edge or non-edge, has to be created. In this study, the optimal thresholding method is used for automatically binarizing I as described in [2]. After the thresholding, isolated edge voxels are removed in order to reduce sensitivity to noise.

Delingette also suggests the use of a two stage technique for recovering the target surface. At the first stage, a coarse mesh with a large α is used for getting close to the target surface. Thereafter, a more fine mesh with smaller α is used for capturing details of it. We also adopted the procedure after few failed attempts to use a single resolution mesh.

3.2 Gradient Vector Flow External Forces

In [16,15] methods for deriving global external forces from image data were proposed. With *gradient vector flow* (GVF) [16] the external force is defined as the vector field $\mathbf{F}_{ext} = \mathbf{f} = (f_1, f_2, f_3) : \mathbb{R}^3 \to \mathbb{R}^3$ minimizing the expression

$$\int_{\mathbb{R}^3} \mu \sum_{i=1}^{3} ||\nabla f_i(\mathbf{x})||^2 + ||\nabla I(\mathbf{x})||^2 ||\mathbf{f}(\mathbf{x}) - \nabla I(\mathbf{x})||^2 d\mathbf{x}, \qquad (5)$$

where μ is a real scalar. A solution can be found by introducing time variable t and finding a steady state solution of

$$\frac{\mathbf{f}(\mathbf{x}; t)}{dt} = \mu \nabla^2 \mathbf{f}(\mathbf{x}; t) - (\mathbf{f}(\mathbf{x}, t) - \nabla I(\mathbf{x})) ||\nabla I(\mathbf{x})||^2, \mathbf{f}(\mathbf{x}; 0) = \nabla I(\mathbf{x}), \quad (6)$$

where the Laplace-operator ∇^2 applies only on the spatial component (i.e $\mathbf{x}$) of $\mathbf{f}$. Generalized gradient vector flow (GGVF) [15] is defined as the equilibrium solution of the following partial differential equation (PDE):

$$\frac{\mathbf{f}(\mathbf{x}; t)}{dt} = g(||\nabla I(\mathbf{x})||) \nabla^2 \mathbf{f}(\mathbf{x}; t) - h(||\nabla I(\mathbf{x})||)(\mathbf{f}(\mathbf{x}, t) - \nabla I(\mathbf{x})), \qquad (7)$$

$$\mathbf{f}(\mathbf{x}, 0) = \nabla I(\mathbf{x}), \qquad (8)$$

where $g(x) = e^{-(\frac{x}{\kappa})^2}, \kappa \in \mathbb{R}$ and $h(x) = 1 - g(x)$.

For finding numerical solutions to the above PDEs, guidelines given in [16,15] are followed. After numerical solutions are found, external forces are normalized to have maximal magnitude of 1. From (discrete) numerical solutions, continuous external force fields are obtained by trilinear interpolation.

4 Energy Based Approach

With the energy based approach one minimizes the energy of the deformable mesh:

$$E(\mathcal{M}) = \frac{1}{N} \sum_{i=1}^{N} (\lambda E_{int}(\mathbf{v}_i) + (1 - \lambda) E_{ext}(\mathbf{v}_i)), \qquad (9)$$

where $\lambda \in [0, 1]$.

The internal energy of $\mathbf{v}_i$ is defined as

$$E_{int}(\mathbf{v}_i) = \frac{||\mathbf{v}_i - \frac{1}{3}\sum_{j=1}^{3}\mathbf{v}_{i_j}||^2}{A(\mathcal{M})}, \tag{10}$$

where $A(\mathcal{M})$ is a measure of area of $\mathcal{M}$. It is computed as the average area of faces of the mesh. Areas of faces of simplex meshes are computed by triangulating them. Note that the internal energy is invariant to scalings, translations and rotations of the mesh. A comparison of (3) and (10) reveals that (3) is the negative of the gradient of the numerator of $E_{int}(\mathbf{v}_i)$ for each i. However, similar result does not hold if we consider the numerator of the internal energy of $\mathcal{M}$ as whole because also $E_{int}(\mathbf{v}_{i_j}), j = 1, 2, 3$, depend on $\mathbf{v}_i$. The external energy is defined as

$$E_{ext}(\mathbf{v}_i) = 1 - I(\mathbf{v}_i). \tag{11}$$

4.1   Dual Surface Minimization

Dual surface minimization (DSM) algorithm was introduced in [12] and refined in [10] for minimization of the energy of deformable surface meshes. It is a generalization of an energy minimization method for active contours [4]. The initialization for the process consists of two surface meshes differing only in size. One of these is placed inside of the sought surface and the other is placed outside of it. Thereafter, the energy of the mesh with higher energy is minimized locally by the greedy algorithm [13] with the constraint that outer mesh must shrink and the inner mesh must grow in size. If the mesh of higher energy is stuck on a local minima, its energy function is modified by adding a penalty for the current position of the mesh [10]. The penalty is increased gradually until the mesh is forced to move from its current position. The whole process continues iteratively until areas of the inner mesh and the outer mesh are approximately equal.

It is necessary to equip meshes with a global position parameter (or moving reference point) if the earlier implementation is used [12]. We tried if the usage of the global position parameter can improve results with the refined implementation [10]. It was found that using meshes equipped with the global position parameter was not worthwhile in our experiments because that did not improve the quality of results and is computationally expensive.

4.2   Minimization Method Based on Genetic Algorithms

A hybrid of real coded genetic algorithms [5] (RCGA) and greedy algorithm [13] for mesh optimization was used in [11]. The algorithm is abbreviated here as GAGR and it is as follows

1. Global minimization of the energy of the mesh by a RCGA;
2. Greedy minimization of the energy of the mesh obtained from the first step;
3. Adaptation of the resolution of the mesh;
4. Minimization of the energy of the adapted mesh for the final solution by the greedy algorithm;

The RCGA uses BLX-0.3 crossover [5], tournament selection and an initial population just like in [11]. Our implementation differs from the original in that the crossover operator is constrained to produce meshes within the image domain. In the original implementation such reasonable constraint was not used and penalty function was applied to solve the problem. Only 100 generations of RCGA are used in the first step for efficiency as in [11].
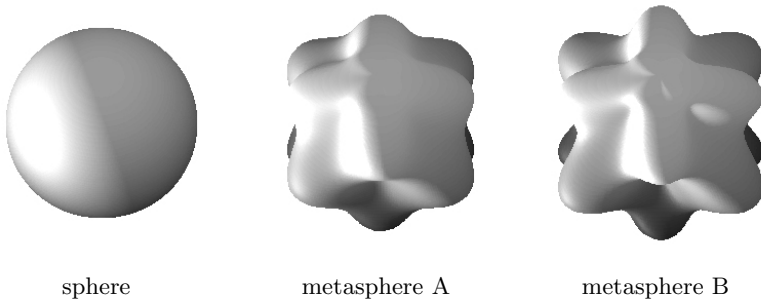

sphere   metasphere A   metasphere B

Fig. 1. Surfaces used in the first experiment

5   Experiments

5.1   Material

Three types of tests were performed for the evaluation. The first experiment was a standard one. First metaspheres [14], see Fig. 1, were drawn to $64 \times 64 \times 64$ grid and then white Gaussian noise was added to the images. Thereafter, images were filtered with a Gaussian filter with the $3 \times 3 \times 3$ kernel and the standard deviation 1.0. The intensity of the true surfaces was 1.

The images for the second kind of tests consisted a true surface of intensity of one and few false surfaces of the intensity of 0.5. Some cross sections of images are shown in Fig. 2.

In the third experiment, boundaries of brain from two FDG (fluorodeoxyglucose) PET (positron emission tomography) images were extracted. An example of a PET image is shown in Fig. 3. Salient image features in this case mean edges which were found by applying a three-dimensional Sobel operator [17]. An edge (magnitude) map from the PET image in Fig. 3 is shown also in Fig. 3.

5.2   Error Measures

With synthetic images, it is possible to evaluate extraction errors also quantitatively. Here two criteria were used: Denote the set of voxels belonging to true
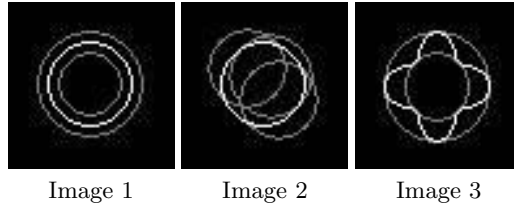
Image 1   Image 2   Image 3

Fig. 2. Central cross sections in xy planes of images for the second experiment.

(digital) surface by TS and the set of voxels belonging to the extracted surface by ES. Furthermore, let the set of voxels inside the true surface be TV and the set of voxels inside the extracted digital surface be EV. Then,

$$\epsilon_1 = 1 - \frac{|TV \cap EV|}{|TV \cup EV|}, \tag{12}$$

$$\epsilon_2 = \max_{X \in TS} \min_{Y \in ES} dist(X, Y), \tag{13}$$

where distance between voxels X and Y ($dist(X, Y)$) is the Euclidean distance between their integer coordinates. The first error measure captures well the goodness of overall result. (Note that the quantity $1 - \epsilon_1$ is known as the Tanimoto coefficient.) The second one reacts also to very local reconstruction errors. This makes it useful in determining if high curvature parts of a surface are extracted well. However, the second measure is not necessarily good for determining how well the surface extraction has succeeded in a global sense.

5.3   Experiment Settings and Implementation

Resolution of Meshes. Meshes of 1280 mexels were used with DSM, GVF and GGVF. With GAGR, at the first stage, meshes of 320 mexels were used. Then the mesh resulting from the resolution adaptation step (Step 3 in the algorithm) was constrained to have 1280 mexels. Same applies for the Delingette's method. Both algorithms adapt the mesh resolution by repeated application of T_2^2 operator defined in [1].

Initializations. With synthetic images, every algorithm except GAGR, was tested with five different initializations. The initializations for the force based methods were spheres all completely outside the true surface. Also initializations inside the true surface were tested with GVF and GGVF but results were not good unless initialization was very close to the target. This is due to shrinking effect of the internal force. For DSM, outer initial surfaces were same than the ones for the force based methods and inner initial surfaces were obtained by scaling from these. With GAGR, an initial population is random, and only one population was used for each image. Similar settings apply for the experiments with PET images, except three ellipsoid initializations per image were tested.
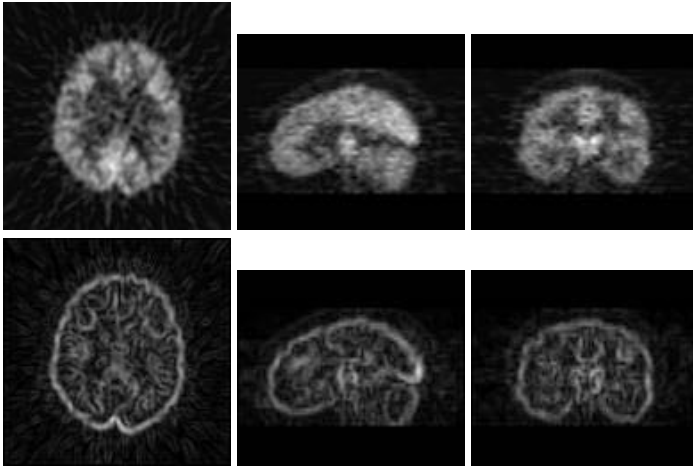
Fig. 3. PET images: Top row (left to right): transaxial, sagittal and coronal views of a FDG-PET image used in the experiments. Bottom row: 3-D Sobel edges from the image in the top row, left to right: Transaxial, sagittal and coronal views.

Parameter Values. The selection of parameter values is often a fundamental issue in implementing deformable models. Here values of as many parameters as possible were fixed before any experiments by using suggestions of the authors of the algorithms. Basically, only values of λ and α were tuned during the experiments. For each method, we tried to find such λ or α that would be suitable for every experiment. Sometimes this was impossible and a change in α or λ between experiments improved results significantly. However, within an experiment all parameter values were fixed since a method is not really automatic if it requires different values of parameters for each input in order to succeed.

The Lagrangian motion was used for force-based techniques in all tests. Also, the Newtonian motion with $\gamma = 0.65$ was studied, but results were generally worse than with the Lagrangian motion. However, the use of the Newtonian motion can offer a speed-up if a large α is applied.

Results with two versions of GVF external forces are reported, one with $\mu = 0.05$ and the other with $\mu = 0.1$, because they were clearly different. Also other values of μ (0.2 and 0.4) were tested but they did not seem to work. With GGVF, $\kappa = 0.05$ suggested in [15] worked well so there was no reason to play with it. Generally, the value of α was 0.1 for GVF and 0.3 for GGVF. With all force based models, β was set so that the maximal magnitude of external forces was 1. With Delingette's method α in the first stage was generally 0.6 and in the second stage 0.1. The values of other parameters were: $\beta_{edge} = 0.0625, \beta_{grad} = 0.15, \beta = 1$. Closest edges to a voxel where looked only within radius of 8 from the voxel. Sometimes, especially with PET images, the binarization of the input image failed completely. Then no edge external force was used and β_{grad} was set

to 0.3. For the energy based approach, only the value of λ was adjusted. It was usually 0.3. For DSM the rest of the parameters (relating mainly to the search spaces) were selected as advised in [10,12].

Complexity. Time consumptions of the algorithms are not given because no attention was paid on how to implement algorithms efficiently, and so listing time consumptions would be misleading. On the average, the method of Delingette and DSM are the fastest algorithms and GAGR is the slowest one. The complexity of GVF and GGVF methods depends heavily on the size of the underlying image in contrast to the other methods. This makes it difficult to evaluate the speed of GVF and GGVF methods as compared to others. On the average, the usage of GVF or GGVF external forces leads to solutions slower than DSM or Delingette's external forces but faster than GAGR.

6   Results

6.1   Results with Synthetic Images

Quantitative results of the first experiments are given in Table 1. The values listed in Table 1 are medians of the error criteria values resulting from different initializations. Some examples of reconstructed surfaces are in Fig. 4. Results were not surprising. All algorithms performed fairly well with images with a sphere in it. In this case, increased noise level most clearly degraded results obtained by DSM. On average, GGVF and GAGR were best methods. With more complex surfaces, DSM performed nearly as well as GGVF and GAGR, which were again best methods. However, there was a larger deviation of error criteria values resulting from different initializations with DSM than with the other methods. The performance of both GVF based algorithms suffered heavily from noise with Metaspheres in the image. As can be seen from Fig. 4, no really good surface reconstruction of Metasphere A was obtained by using any of the algorithms when the noise variance was 0.6. However, the results obtained by GAGR, DSM, GGVF and external force of Delingette were acceptable. This was not the case with GVF external forces.

Deligette's external force led to the surface shrunk to a point from some of the initializations with noiseless images although it produced quite good results with noisy images. This can avoided by carefully tuning the parameter α, but that might require a-priori knowledge about the signal to noise ratio of the image.

The error criteria values from the second experiment can be found from Table 2. Again, the values are medians of the ϵ_2 values resulting from different initializations. The findings of the experiment were interesting. Meshes with GGVF external forces stuck with outermost false surface. Changing values of κ and α did not help. GVF with $\mu = 0.1$ produced best results in this experiment. The results with GVF with $\mu = 0.05$ and $\alpha = 0.1$ were worse as can be seen from Table 2. However, GVF with $\mu = 0.05$ and $\alpha = 0.3$ gave results similar to those with GVF and $\mu = 0.1$.

The method of Delingette was also quite good in this experiment. Surprisingly, although the binarization algorithm labeled all surfaces, true or false, as edges, results with the edge external force were better than those with no edge external force and $\beta_{grad} = 0.3$.

DSM was successful with Image 1 and in some extent with Image 3. The extraction of true surface from Image 2 failed. The reason for failure was that the algorithm failed to converge because of the oscillation. This problem was also noted in [10] and an effort were made to prevent oscillations in this study. GAGR optimization produced results almost as good as those obtained with GVF and $\mu = 0.1$. Only with Image 3, surface extraction has failed a little bit as ϵ_2 value in Table 2 reveals.

Table 1. Error criteria values from the first set of tests. Medians of values from different initializations are shown. Symbol σ^2 stands for variance of Gaussian noise. GVF 0.05 means GVF with $\mu = 0.05$, and similarly GVF 0.1 means GVF with $\mu = 0.1$. Parameter values were as listed in Sect. 5.3.

measure	surface	σ^2	Method					
			GVF 0.05	GVF 0.1	GGVF	Delingette	DSM	GAGR
	sphere	0	0.03	0.03	0.03	0.08	0.03	0.05
		0.2	0.09	0.11	0.05	0.07	0.06	0.06
		0.6	0.09	0.12	0.06	0.08	0.14	0.06
		1	0.13	0.17	0.06	0.08	0.17	0.07
		1.4	0.13	0.17	0.07	0.13	0.21	0.07
	metasphere A	0	0.03	0.03	0.02	0.09	0.03	0.06
		0.2	0.11	0.16	0.05	0.09	0.02	0.07
ϵ_1		0.6	0.16	0.24	0.10	0.11	0.10	0.08
		1.0	0.20	0.26	0.14	0.12	0.14	0.11
	metasphere B	0	0.07	0.07	0.06	1	0.07	0.10
		0.2	0.30	0.37	0.13	0.19	0.11	0.16
		0.6	0.27	0.38	0.19	0.21	0.18	0.20
		1.0	0.27	0.36	0.24	0.26	0.32	0.22
	sphere	0	1.4	1.4	1.4	1.4	2.2	2.2
		0.2	1.7	2.2	1.4	1.7	2.0	1.4
		0.6	2.0	2.2	2.0	2.4	2.4	2.2
		1	2.8	3.0	1.7	3.0	4.5	1.7
		1.4	2.7	3.0	1.4	3.6	4.2	2.2
	metasphere A	0	1.4	1.4	1.4	4.9	2.2	1.7
		0.2	4.0	5.1	3.0	2.4	2.0	2.2
ϵ_2		0.6	4.6	7.0	5.8	3.3	3.2	3.0
		1.0	5.4	6.3	5.7	5.4	6.1	4.4
	metasphere B	0	3	2.8	2.2	-	3.2	3.5
		0.2	9.3	10	6.1	6.4	3.0	8.5
		0.6	8.6	10	7.3	8.5	6.7	7.3
		1.0	6.5	10	10	9.1	10.3	7.3

Table 2. Error values from the second set of tests. Listed values are medians of the error criteria obtained from different initializations. Parameter values were as listed in Sect. 5.3.

measure	image no.	Method					
		GVF 0.05	GVF 0.1	GGVF	Delingette	DSM	GAGR
	1	0.16	0.03	0.50	0.07	0.04	0.05
ϵ_1	2	0.06	0.05	0.51	0.07	0.34	0.05
	3	0.07	0.02	0.42	0.09	0.12	0.10
	1	3.6	1.4	4.4	3.0	1.7	2.0
ϵ_2	2	2.0	2.2	10	1.7	9.6	2.2
	3	5.7	1.4	7.3	3.2	4.6	7.7

6.2   Results with Medical Images

For PET images there were two methods above others. GGVF and DSM produced excellent results with all initializations and both images. However, with GGVF the success was achieved only after changing value of α to 0.1. GGVF with $\alpha = 0.3$ worked well only with one of the images. DSM was good with both images and pre-defined set of parameters. GGVF results were slightly more accurate than the ones obtained with DSM. See Fig. 5 for examples. With GAGR we had some success in this experiment without tuning parameters, however resulting surfaces were clearly less accurate (see Fig. 5) than with the methods mentioned above. Using $\lambda = 0.4$ improved the resulting surfaces, but not much. Delingette's technique produced some moderate results after tuning of value of α in the both stages of the two stage algorithm. But further adjustment of parameter values would still be required in order to have acceptable results. Also best parameter values varied from image to image and from initialization to initialization. See Fig. 6. It was necessary to use the gradient external force only, since the thresholding algorithm did not perform well. However, thresholding original PET-image and then finding edges is probably better alternative than simply thresholding the gradient-image (as we did). GVF external forces had the worst performance of the methods in this experiment, even adjusting value of α would not help much. See Fig. 5 for the best result obtained by GVF.

7   Discussion

We have compared experimentally few recent algorithms based on deformable meshes for the surface extraction from noisy volumetric images. As one could have expected, no universally best method for controlling the deformation of the mesh was found. It depends on the application which algorithm is the best. In general, GAGR seems to be the most reliable choice: It gave good results in synthetic image experiments and errors in the PET image experiment were not large. However, if it is known in advance that the target surface is the
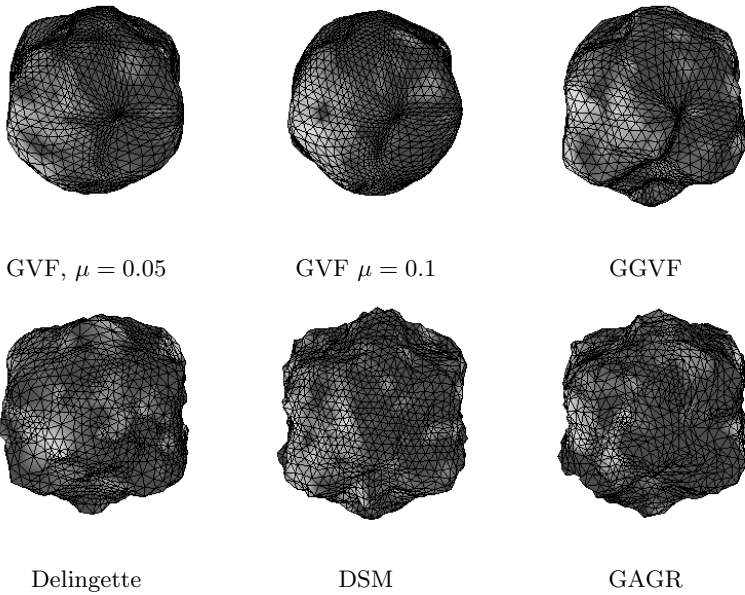
Fig. 4. Extracted Metasphere A from the image of noise variance of 0.6 using different methods. Surfaces are from initializations that led to the median value of the ϵ_1.

outermost surface in the image as was the case in the PET image experiment, then algorithms like GGVF or DSM - which can actually gain from the situation - are the ones to be preferred. GAGR as general purpose optimization algorithm does not have the capability to take advantage of structural a-priori information about the image unless it is coded into the energy function.

DSM and GGVF were also reliable choices, but they also have weaknesses as the second set of tests with synthetic images proved. GGVF external forces can cope with random noise sufficiently well, but are not able to handle false surfaces in the image. In the case of false surfaces, meshes with GGVF external forces tended to stuck with the outermost "strong enough" surface in the image. The problem of the DSM was that it was not always able to converge: the mesh with higher energy may stick oscillating between few surface positions. This is clearly an implementational problem, but solving it completely and efficiently could be challenging. The implementation of DSM from [12] does probably not impose oscillation problems but has other disadvantages compared to the implementation from [10].

GVF external forces worked well when a simple surface, such as a sphere, was to be extracted. However, when the surface in the image was more complex and the image was even slightly noisy we were not able to get good results with GVF external forces. This is due to the regularizing component of (5) which tends to blur the surface details, see [15]. GVF external forces failed with PET images,
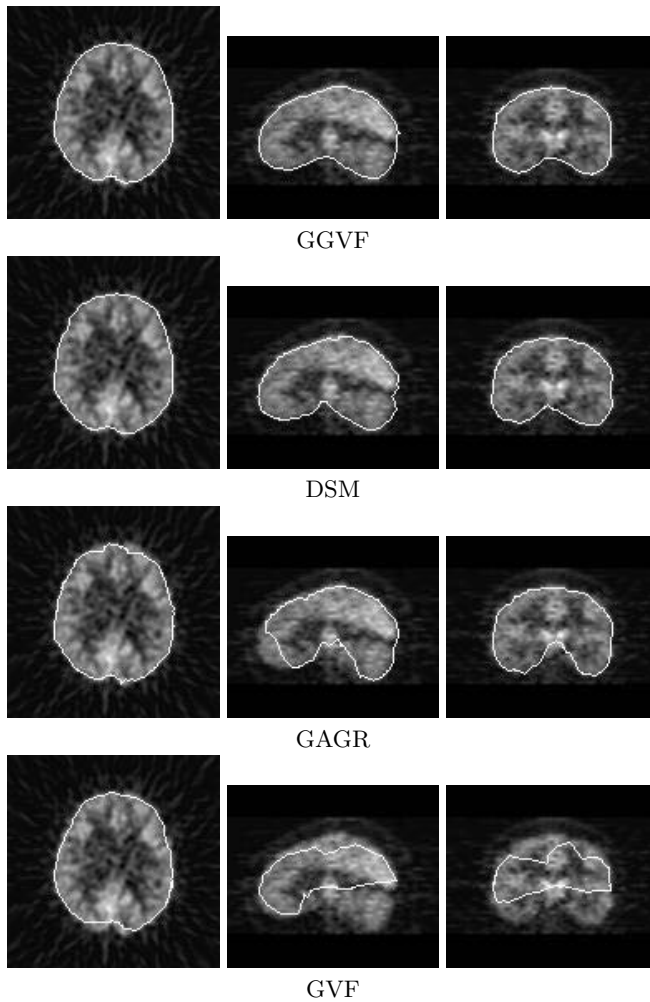
GGVF

DSM

GAGR

GVF

Fig. 5. Cross-sections of the extracted brain surfaces from a PET image. From left to right: transaxial view, sagittal view, coronal view. Result with GVF was obtained by using the best set of parameter values ($\alpha = 0.05, \mu = 0.05$) and the best initialization. Other results were obtained with pre-defined parameter values and results from other initializations look similar.

where the problem is intensity inhomogeneity of the target surface in addition to noise. However, GVF external forces worked well in extraction of the correct surface from images where also false surfaces were present.

The external forces of Delingette turned out to do well in synthetic image experiments. The extraction results were good but generally not the most accurate ones. In the PET image experiment, we were not able to obtain good results
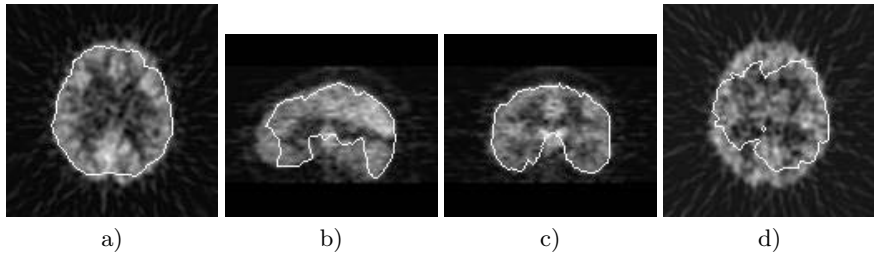
<div style="text-align:center">a)   b)   c)   d)</div>

Fig. 6. Results with external forces of Delingette. a) b) and c): The result from the best initialization with a PET image, transaxial, sagittal and coronal views. Parameter $\alpha = 0.3$ at the first stage and $\alpha = 0.1$ at the second stage. d) The transaxial view of a result with the same initialization but a different image than for the result shown in a),b) and c).

with this external force model. The results could maybe be improved by using a more advanced thresholding method than the one used in this study and fine tuning the parameter values. Indeed, the results obtained by using Delingette's external forces were sensitive to parameter values for the deformable mesh. In fact, this is also the major difference between force based and energy based approach. The energy based scheme is less sensitive to values of parameters, which makes it easier to select them well. On the other hand, the force based approach has an advantage of not discretizing the search space, what often leads visually more pleasant surface reconstructions.

To conclude, there is no optimal deformable meshing scheme which upper-hands the others in all applications. This study has highlighted strengths and weaknesses of recent methods to guide the deformation process in a general context. Because of generic nature of our experiments, we have been able to observe common characteristics of each method. Hopefully, the study will be a useful reference to those applying deformable meshes.

References

[1] H. Delingette. General object reconstruction based on simplex meshes. *International Journal of Computer Vision*, 32:111–142, 1999.
[2] R.C. Gonzales and R.W. Woods. *Digital Image Processing.* Addison-Wesley, Reading, MA, 1992.
[3] S.R. Gunn. *Dual Active Contour Models for Image Feature Extraction.* PhD thesis, University of Southampton, 1996.

[4] S.R. Gunn and M.S. Nixon. A robust snake implementation: a dual active contour. *IEEE Transactions on Pattern Analysis and Machine Intelligence*, 19(1), 1997.

[5] F. Herrera, M. Lonzano, and J. L. Verdegay. Tackling real-coded genetic algorithms: Operators and tools for behaviorial analysis. *Artificial Intelligence Review*, 12(4), 1998.

[6] M. Kass, A. Witkin, and D. Terzopoulos. Snakes: Active contour models. *International Journal of Computer Vision*, 1(4):321 – 331, 1988.

[7] J.-O. Lachaud and A. Montanvert. Deformable meshes with automated topology changes for coarse-to-fine three-dimensional surface extraction. *Medical Image Analysis*, 3(2), 1998.

[8] T. McInerney and D. Terzopoulos. Deformable models in medical image analysis: A survey. *Medical Image Analysis*, 2(1), 1996.

[9] J. Montagnat, H. Delingette, N. Scapel, and N. Ayache. Representation, shape, topology and evolution of deformable surfaces. application to 3D medical image segmentation. Technical report, INRIA, 2000.

[10] U. Ruotsalainen, J. Mykkänen, J. Luoma, J. Tohka, and S. Alenius. Methods to improve repeatability in quantification of brain PET images. In *World Congress on Neuroinformatics: Part II Proceedings, ARGESIM Report no. 20*, pages 659 – 664, 2001.

[11] J. Tohka. Global optimization of deformable surface meshes based on genetic algorithms. In *Proc. of 11th International Conference on Image Analysis and Processing, ICIAP01*, pages 459 – 464, 2001.

[12] J. Tohka and J. Mykkänen. Deformable mesh for automated surface extraction from noisy images. Submitted to IEEE Transactions on Medical Imaging, 2001. Available online http://www.cs.tut.fi/ jupeto/dmnoisy.pdf.

[13] D.J. Williams and M. Shah. A fast algorithm for active contours and curvature estimation. *CVGIP: Image Understanding*, 55(1):14 – 26, 1992.

[14] C. Xu. *Deformable Models with Application to Human Celebral Cortex Reconstruction from Magnetic Resonance Images*. PhD thesis, the Johns Hopkins University, 1999.

[15] C. Xu and J.L Prince. Generalized gradient vector flow external forces for active contours. *Signal Processing*, 71(2), 1998.

[16] C. Xu and J.L. Prince. Snakes, shapes and gradient vector flow. *IEEE Transactions on Image Processing*, 7(3), 1998.

[17] S. Zucker and R. Hummel. A three-dimensional edge operator. *IEEE Transactions on Pattern Analysis and Machine Intelligence*, 3(3), 1981.